Optik - International Journal for Light and Electron Optics 224 (2020) 165748

Contents lists available at ScienceDirect

Optik

journal homepage: www.elsevier.com/locate/ijleo

Original research article

Large rigid-body displacement parameters extraction of segmented mirror in pose co-phasing adjustment simulation analysis using constrained optimization method

Huisheng Yang [a,*], Xuejun Zhang [a], Baixu Liu [b], Xinyuan Pang [a], Zhilai Li [a]

[a] Changchun Institute of Optics, Fine Mechanics and Physics, Chinese Academy of Sciences, Changchun, 130033, China
[b] FAW-Volkswagen Automotive Co., LTD, Changchun, 130000, China

ARTICLE INFO

Keywords:
Segmented mirror
Finite element analysis
Co-phasing adjustment
Rigid-body displacement
Parameter extraction

ABSTRACT

Large rigid-body displacement parameters within finite element analysis results are hard to be extracted. We propose an algorithm to solve this problem. Firstly, the constraint equations are established. The linear coordinate equations and objective function are then constructed. By using Lagrange multiplier method and Taylor series expansion, the solution algorithm is derived. Numerical simulation results reveal that the algorithm can separate ultra-large rigid-body rotation within the range of ±180° with the accuracy of less than 1‰ and the solving efficiency is more than twice that of the trigonometric function method. The application experiments show that the algorithm can meet the actual engineering requirements.

1. Introduction

In order to break through the limitation of spacecraft on the space-based observatory aperture, the deployable optical system using segmented primary mirror emerged as the times require, and it has attracted great attention of all countries in the world [1–5]. The most representative example is the James Webb Space Telescope (JWST) whose primary mirror is composed of 18 segmented mirrors [6]. However, the deployable optical system also provides huge challenges while bringing the aperture merit. Among them, the co-phasing adjustment of the segments is one of the most critical challenges, which determines the success or failure of the mission.

The primary mirror co-phasing is to adjust the position and attitude of segments with high precision by the phasing mechanism, so that all segments can form an optical surface which can provide the imaging ability of the equivalent design aperture [7–11]. This is a challenging task, which requires phasing devices achieving nano-positioning accuracy within millimeter range of motion. In order to achieve this target, it is necessary to adopt the iterative optimization method based on finite element analysis result. However, the analysis result can only give the deformation map, and cannot separate the rigid-body displacement parameters which are the basic data for the design of the phasing mechanism. This is extremely inconvenient for the hexapod design and optimization.

The rigid-body displacement separation usually adopts a trigonometric function model which is established according to the coordinate transformation principle. There are two methods to solve this trigonometric function model. The first is commonly used [12–15]. In order to reduce the solution difficulty, the model is linearized according to the small-angle approximation theory, $\sin\theta \approx \theta$ and $\cos\theta \approx 1$. This method has good convergence and computational complexity. But the disadvantages are also obvious. Firstly, this method is only applicable to the parameters extraction for tiny rigid-body displacement. Secondly, its accuracy is not constant, but

* Corresponding author.
E-mail address: yanghuisheng@126.com (H. Yang).

https://doi.org/10.1016/j.ijleo.2020.165748
Received 5 July 2020; Accepted 2 October 2020
Available online 8 October 2020

decreases with the increase of the rigid-body rotation. The second method, called TFM (trigonometric function method), is not commonly used because of the large calculation. It does not perform a linear approximation, but directly solve the model by using the least-squares iteration. This method can separate the angular displacement within $\pm 180^{\circ}$, but needs to derive the partial derivatives of the advanced nonlinear equations, and a large number of trigonometric functions are calculated for each iteration. Therefore, its solution efficiency is terrible. In addition, the method does not converge for some special conditions, for example, the triaxial rotation angles are -90° respectively.

In order to solve the problem that large rigid-body displacement parameters in the finite element analysis results are hard to be extracted, a high precision and efficient rigid-body displacement extraction algorithm is proposed based on constrained optimization method. The constraint equations are established, by analyzing the properties of coordinate transformation matrix. The linear coordinate equations of deformed nodes and the objective function are constructed using the generalized rigid body displacement vector. By using Lagrange multiplier method and Taylor series expansion, the solution method of these linear equations is derived, and the solution program is developed. Finally, this algorithm is compared with the trigonometric functions method through numerical simulations and application experiments.

2. Basic theory

2.1. Constraint equations

The spatial position and attitude can be described by a coordinate system fixed to the segmented mirror. Once the system is established, the position of any point in the segment can be described by a 3×1 vector. According to the homogeneous coordinate transformation theory, the homogeneous coordinate vector of any point in two coordinate systems has the following correlation:

$$[{}^{A}x, {}^{A}y, {}^{A}z, 1]^{T} = A[{}^{B}x, {}^{B}y, {}^{B}z, 1]^{T} \tag{1}$$

where $[{}^{A}x, {}^{A}y, {}^{A}z, 1]^{T}$ is the homogeneous coordinate vector defined in the coordinate system {A}. $[{}^{B}x, {}^{B}y, {}^{B}z, 1]^{T}$ is the homogeneous coordinate vector defined in the coordinate system {B}. **A** is the homogeneous coordinate transformation matrix which is composed of the attitude transformation matrix R and the position translation vector T:

$$\mathbf{A} = \begin{bmatrix} R & T \\ 0 & 1 \end{bmatrix} \tag{2}$$

For coordinate transformation between Cartesian coordinate systems, the attitude matrix can be expressed as:

$$R = \begin{bmatrix} n_x & o_x & a_x \\ n_y & o_y & a_y \\ n_z & o_z & a_z \end{bmatrix} \tag{3}$$

where $[n_x, n_y, n_z]^{T}$, $[o_x, o_y, o_z]^{T}$ and $[a_x, a_y, a_z]^{T}$ are three unit principal vectors and orthogonal to each other.

Therefore, the constraint equations can be written as:

$$n_x^2 + n_y^2 + n_z^2 = 1 \tag{4}$$

$$o_x^2 + o_y^2 + o_z^2 = 1 \tag{5}$$

$$a_x^2 + a_y^2 + a_z^2 = 1 \tag{6}$$

$$n_x o_x + n_y o_y + n_z o_z = 0 \tag{7}$$

$$o_x a_x + o_y a_y + o_z a_z = 0 \tag{8}$$

$$n_x a_x + n_y a_y + n_z a_z = 0 \tag{9}$$

2.2. Derivation of rigid-body displacement parameters extraction algorithm

Po_i is the original position vector of the node i on the segmented mirror surface.

$$Po_i = [\, xo_i \quad yo_i \quad zo_i \,]^{T} \tag{10}$$

and Pd_i is the post-deformation position vector of the node i on the segmented mirror surface, which is given in the analysis result.

$$Pd_i = [\, xd_i \quad yd_i \quad zd_i \,]^{T} \tag{11}$$

It should be noted that the vector Pd_i contains not only the rigid-body displacement deformation, but also the surface distortion. The rigid-body displacement deformation does not change the relative position between nodes, which is beneficial for the parameters

extraction, while the surface distortion will change the relative position between nodes, which is harmful.

The TFM uses the RPY rotation sequence in robotics to generate the attitude transformation matrix (Eq. (3)), which can reduce the number of variables from the original 9 to 3. This algorithm is intuitive and easy to understand, but has significant disadvantage: It needs to derive the partial derivatives of the advanced nonlinear equations, calculate a large number of trigonometric functions for each iteration, and do not converge for some special conditions, for example, the triaxial rotation angle is -90 degrees.

In order to avoid the above problems, a linear model based on generalized rigid-body displacement vector u is proposed:

$$P_i = \begin{bmatrix} x_i \\ y_i \\ z_i \end{bmatrix} = \begin{bmatrix} n_x xo_i + o_x yo_i + a_x zo_i + t_x \\ n_y xo_i + o_y yo_i + a_y zo_i + t_y \\ n_z xo_i + o_z yo_i + a_z zo_i + t_z \end{bmatrix} \tag{12}$$

and:

$$u = [n_x, n_y, n_z, o_x, o_y, o_z, a_x, a_y, a_z, t_x, t_y, t_z,]^T \tag{13}$$

where P_i is the position vector of node Po_i after rigid-body motion u.

Because of the factors such as fitting residual, surface distortion and analysis errors, P_i is not equal to Pd_i, and the residual v is:

$$v_i = Pd_i - P_i = \begin{bmatrix} xd_i - n_x xo_i - o_x yo_i - a_x zo_i - t_x \\ yd_i - n_y xo_i - o_y yo_i - a_y zo_i - t_y \\ zd_i - n_z xo_i - o_z yo_i - a_z zo_i - t_z \end{bmatrix} \tag{14}$$

The objective function can be written as:

$$Q(u) = v^T v \tag{15}$$

According to the least squares theory, when u takes the best value, the objective function is minimum. In this way, the parameters extraction process can be transformed into a constrained optimization problem:

$$\begin{cases} \min Q(u) \\ \varphi_i(u) = 0 \quad i = 1, 2, 3, 4, 5, 6 \end{cases} \tag{16}$$

where

$$\varphi_1(u) = n_x^2 + n_y^2 + n_z^2 - 1 = 0 \tag{17}$$

$$\varphi_2(u) = o_x^2 + o_y^2 + o_z^2 - 1 = 0 \tag{18}$$

$$\varphi_3(u) = a_x^2 + a_y^2 + a_z^2 - 1 = 0 \tag{19}$$

$$\varphi_4(u) = n_x o_x + n_y o_y + n_z o_z = 0 \tag{20}$$

$$\varphi_5(u) = n_x a_x + n_y a_y + n_z a_z = 0 \tag{21}$$

$$\varphi_6(u) = o_x a_x + o_y a_y + o_z a_z = 0 \tag{22}$$

According to the Lagrange multiplier method, the objective function with constraints can be expressed as:

$$E(u, \lambda) = Q(u) + 2\lambda^T \varphi(\varsigma) \tag{23}$$

where $\lambda = [\lambda_1, \lambda_2, \lambda_3, \lambda_4, \lambda_5, \lambda_6]^T$.

According to the extremum condition, we have:

$$\frac{\partial E(u, \lambda)}{\partial u} = -2v^T \cdot \begin{bmatrix} \dfrac{\partial f_1(u)}{\partial u} \\ \vdots \\ \dfrac{\partial f_n(u)}{\partial u} \end{bmatrix} + 2\lambda^T \begin{bmatrix} \dfrac{\partial \varphi_1(u)}{\partial u} \\ \vdots \\ \dfrac{\partial \varphi_m(u)}{\partial u} \end{bmatrix} = 0 \tag{24}$$

$$\frac{\partial E(u, \lambda)}{\partial \lambda} = 2\varphi(u) = 0 \tag{25}$$

where

$$f_i(u) = \begin{bmatrix} n_x xo_i + o_x yo_i + a_x zo_i + t_x \\ n_y xo_i + o_y yo_i + a_y zo_i + t_y \\ n_z xo_i + o_z yo_i + a_z zo_i + t_z \end{bmatrix} \tag{26}$$

Let:

$$F = \begin{bmatrix} \dfrac{\partial f_1(u)}{\partial u} \\ \vdots \\ \dfrac{\partial f_n(u)}{\partial u} \end{bmatrix};\ M = \begin{bmatrix} \dfrac{\partial \varphi_1(u)}{\partial u} \\ \vdots \\ \dfrac{\partial \varphi_m(u)}{\partial u} \end{bmatrix} \tag{27}$$

And:

$$F = \begin{bmatrix} \dfrac{\partial f_1}{\partial u_1} & \dfrac{\partial f_1}{\partial u_2} & \cdots & \dfrac{\partial f_1}{\partial u_{12}} \\ \dfrac{\partial f_2}{\partial u_1} & \dfrac{\partial f_2}{\partial u_2} & \cdots & \dfrac{\partial f_2}{\partial u_{12}} \\ \vdots & \vdots & \ddots & \vdots \\ \dfrac{\partial f_{3n}}{\partial u_1} & \dfrac{\partial f_{3n}}{\partial u_2} & \cdots & \dfrac{\partial f_{3n}}{\partial u_{12}} \end{bmatrix} \tag{28}$$

$$M = \begin{bmatrix} \dfrac{\partial \varphi_1}{\partial u_1} & \dfrac{\partial \varphi_1}{\partial u_2} & \cdots & \dfrac{\partial \varphi_1}{\partial u_{12}} \\ \dfrac{\partial \varphi_2}{\partial u_1} & \dfrac{\partial \varphi_2}{\partial u_2} & \cdots & \dfrac{\partial \varphi_2}{\partial u_{12}} \\ \vdots & \vdots & \ddots & \vdots \\ \dfrac{\partial \varphi_6}{\partial u_1} & \dfrac{\partial \varphi_6}{\partial u_2} & \cdots & \dfrac{\partial \varphi_6}{\partial u_{12}} \end{bmatrix} \tag{29}$$

Therefore, Eq. (24) can be simplified as:

$$-2v^T \cdot F + 2\lambda^T M = 0 \tag{30}$$

If after k iterations, a set of solutions $u^{(k)}, \lambda^{(k)}$ is found. Perform Taylor series extension of $\varphi(u)$ at $u^{(k)}$, and ignore the high level terms. The constraint equation can be expressed as:

$$\varphi(u) = \varphi(u^{(k)}) + M^{(k)}(u^{(k+1)} - u^{(k)}) \tag{31}$$

It can be obtained from Eqs. (17)–(22):

$$\varphi(u^{(k)}) + M^{(k)}(u^{(k+1)} - u^{(k)}) = 0 \tag{32}$$

Similarly, perform Taylor series extension of $v(u)$ at $u^{(k)}$, and ignore the high level terms. So the residual of the $(k+1)^{\text{th}}$ iteration can be written as:

$$v(u^{(k+1)}) = v(u^{(k)}) - F(u^{(k+1)} - u^{(k)}) \tag{33}$$

Connect with Eq. (29) and the generalized rigid-body displacement vector of the $(k+1)^{\text{th}}$ iteration is:

$$u^{T(k+1)} = u^{T(k)} + [v^T(u^{(k)}) \cdot F - \lambda_T^{(k)} M^{(k)}] \cdot (F^T \cdot F)^{-1} \tag{34}$$

Connect with Eq. (30) and the Lagrange multiplier of the k^{th} iteration is:

$$\lambda_T^{(k)} = [\varphi_T^{(k)} + v_T^{(k)} \cdot F \cdot (F^T \cdot F)^{-1} M_T^{(k)}] \cdot [M^{(k)} \cdot (F^T \cdot F)^{-1} M_T^{(k)}]^T \tag{35}$$

Substitute Eq. (35) into Eq. (34), we can calculate the new generalized rigid-body displacement vector (GRDV), and carry out the next iteration.

Finally, the parameters extraction method based on the constrained-least-squares optimization method (COM) can be expressed as:

$$\begin{cases} \boldsymbol{u}^{(0)} = 0 (\text{初始向量}) \\ \boldsymbol{v}^{(k)} = \boldsymbol{P}d - f(\boldsymbol{u}^{(k)}) \\ \boldsymbol{\lambda}^{T(k)} = [\boldsymbol{\varphi}^{T(k)} + \boldsymbol{v}^{T(k)} \cdot \boldsymbol{F} \cdot (\boldsymbol{F}^T \cdot \boldsymbol{F})^{-1} \boldsymbol{M}^{T(k)}] \cdot [\boldsymbol{M}^{(k)} \cdot (\boldsymbol{F}^T \cdot \boldsymbol{F})^{-1} \boldsymbol{M}^{T(k)}]^T \\ \Delta \boldsymbol{u}^T = [\boldsymbol{v}^T(\boldsymbol{u}^{(k)}) \cdot \boldsymbol{F} - \boldsymbol{\lambda}^{T(k)} \boldsymbol{M}^{(k)}] \cdot (\boldsymbol{F}^T \cdot \boldsymbol{F})^{-1} \\ \boldsymbol{u}^{(k+1)} = \boldsymbol{u}^{(k)} + \Delta \boldsymbol{u} \end{cases} \tag{36}$$

3. Solving program

After the parameters extraction algorithm is completed, a solving program is developed. The flow chart is shown in Fig. 1. It can be seen that the ultra-large-scale Jacobian matrix F is only calculated once during entire solution process, and so does the diagonal matrix F^TF. In addition, the computational complexity of matrix F is very low, only assigning Po_i to F. The Jacobian matrix M, which needs to be updated for each iteration, is very small in scale, and the update is to replace the old GRDV with the new. Therefore, compared with the TFM, the COM has the characteristics of simple to solve, less calculation and high efficiency.

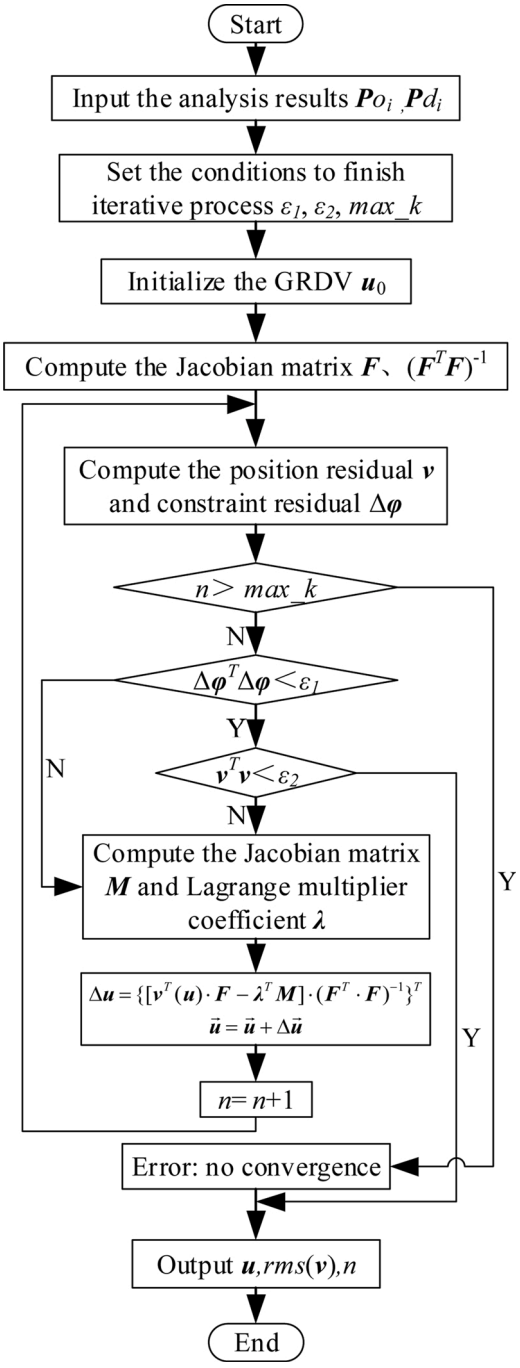

Fig. 1. The flow chart of the COM algorithm.

4. Numerical simulations

After the solving program is completed, numerical simulations are achieved to verify the validity of the program. The simulations adopt the following procedures: Firstly, produce n feature points which are evenly distributed on a spherical mirror with diameter 200 mm and radius of curvature 1000 mm. The nominal position of these points are indicated by $\vec{p}$. Then, design the GRDV $\vec{u}_v$ to be verified, calculate these feature points position $\vec{p}d$ after rigid-body motion $\vec{u}_v$ according to the coordinate transformation. It should be noted that the vector $\vec{u}_v$ is arbitrary and can be generated randomly or manually. Finally, the position vectors before and after the rigid-body motion are substituted into the solving program, and the rigid-body displacement $\vec{u}$ is obtained. Comparing $\vec{u}$ with $\vec{u}_v$, we can verify the validity and accuracy of the program.

The mirror surface used in numerical simulations is shown in Fig. 2, on which there are 4936 feature points. It should be noted that the program can be applied not only to the regular surface, but also to irregular surface, bodies and discrete points, although the numerical simulations is performed on a spherical surface.

In order to comprehensively test the program, 10 sets of rigid-body displacement vectors are produced using a random program. The 10 sets of vectors are shown in Table 1. The rigid-body rotation is described using the RPY (roll, pitch, yaw) rotation sequence.

4.1. Simulations without interference

The simulation result without interference is shown in Table 2. It can be seen from Table 2 that the program can separate the rigid-body displacement with errors close to zero.

4.2. Simulations with uniform distribution interference

In order to verify the anti-interference ability of the algorithm, a uniformly distributed interference, which can simulate the finite element simulation analysis errors, is added. For comparison purpose, the parameters to be verified are the same as those in Table 1. Fig. 3 shows the uniform distribution interference with a peak-to-valley value of 0.02 mm, and the simulation result under the interference is shown in Table 3.

Form Table 3, we can discover the following laws: Firstly, compared with the simulations without interference, the accuracy for the simulations with the uniform distribution interference has decreased significantly, but still is better than 2e-3‰. Secondly, for the 10 sets of rigid body displacement simulations with significant differences, the COM program has the same residual (rms 3.3e-3 mm), which indicates that its accuracy consistency is excellent. Finally, the residual is at the same level as the interference (rms 5.8e-3 mm), which states that the algorithm has sufficient solving accuracy to completely separate the deformation caused by the rigid-body displacement. The reason why the residual is slightly smaller than the interference is because the rigid-body motion will partially compensate the surface distortion. And the program can automatically calculate this optimal compensation value, which becomes part of the GRDV solving residual. All the above laws prove that the COM algorithm proposed in this paper is effective.

4.3. Simulations with Zernike polynomial distribution interference

Zernike polynomials are usually used to evaluate the quality of optical surface in optical engineering. The simulations with 0.01 mm Z4 to Z13 Zernike polynomials interference (shown in Fig. 4), which is used to simulate the surface distortion, are achieved, and the verification result is shown in Table 4.

From Table 4, we can find the similar laws as Table 3. It needs to be additionally stated that because the rigid-body motion has greater compensation ability on the Zernike polynomials, the parameters extraction precision is slightly lower than that for uniform distribution interference. But the program accuracy is still better than 0.8‰, which is higher than the finite element simulation analysis

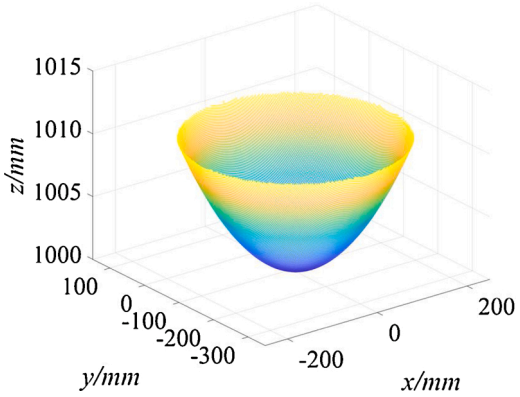

Fig. 2. The diagram of the spherical surface without deformation.

Table 1
Ten groups of rigid-body displacement conditions to be verified.

Number	rigid-body translation/*mm*			rigid-body rotation /°		
	t_x	t_y	t_z	θ_x	θ_y	θ_y
1	−381	391	429	150	156	−120
2	−2	459	−150	−77	−133	37
3	460	47	−303	93	25	−85
4	−160	−361	−249	123	−18	−108
5	85	−351	116	−43	−176	68
6	−276	−242	−27	−83	−35	−115
7	251	341	−148	−153	−122	−18
8	−245	−246	331	−161	106	−150
9	6	314	85	11	−68	−98
10	199	−256	50	101	10	149

Table 2
Verification results of the COM program under no interference.

Number	Translation errors/*mm*			Rotation errors /°			*rms*(*v*)/*mm*
	Δt_x	Δt_y	Δt_z	$\Delta\theta_x$	$\Delta\theta_y$	$\Delta\theta_y$	
1	0	0	0	7.e-15	0	0	2.e-13
2	−1.e-13	−1.e-13	−6.e-14	−8.e-15	0	0	1.e-13
3	−6.e-14	7.e-15	0	−1.e-14	−1.e-14	−1.e-14	2.e-13
4	0	−1.e-13	0	−2.e-13	0	2.e-14	2.e-13
5	**3.e-13**	0	**-2.e-13**	−3.e-14	0	7.e-15	2.e-13
6	0	0	−7.e-15	5.e-17	0	3.e-16	4.e-14
7	2.e-13	0	0	3.e-14	**-4.e-13**	**3.e-14**	6.e-13
8	0	−3.e-14	0	−9.e-16	−1.e-14	0	9.e-14
9	3.e-14	0	−4.e-14	0	0	0	1.e-13
10	−1.e-13	0	−6.e-14	−4.e-15	0	0	8.e-14

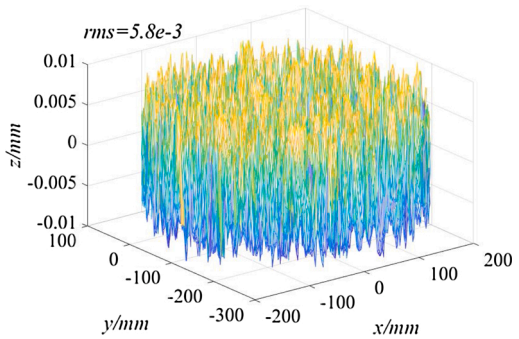

Fig. 3. The diagram of the uniform distribution noise with peak-to-valley value of 0.02mm.

Table 3
Verification results of the COM program under uniform distribution interference.

Number	Translation errors/*mm*			Rotation errors /°			*rms*(*v*)/*mm*
	Δt_x	Δt_y	Δt_z	$\Delta\theta_x$	$\Delta\theta_y$	$\Delta\theta_y$	
1	−7.7e-5	5.3e-5	−6.1e-5	8.9e-7	−5.9e-6	−1.7e-5	3.3e-3
2	2.9e-5	5.3e-5	9.4e-5	1.7e-5	−3.8e-6	−1.2e-5	3.3e-3
3	−3.9e-7	−7.4e-5	8.4e-5	1.3e-5	1.1e-5	−1.2e-5	3.3e-3
4	1.2e-6	**-1.1e-4**	3.1e-5	−8.6e-6	**-2.1e-5**	−8.6e-6	3.3e-3
5	−8.3e-5	5.5e-6	7.4e-5	**2.1e-5**	9.2e-6	−6.1e-6	3.3e-3
6	1.2e-6	**1.1e-4**	−3.1e-5	−1.3e-5	9.0e-13	−1.5e-5	3.3e-3
7	−4.9e-6	−9.8e-5	5.3e-5	−1.1e-5	1.3e-5	−1.3e-5	3.3e-3
8	−1.3e-5	1.1e-4	−2.0e-5	−1.1e-5	−9.0e-7	−1.6e-5	3.3e-3
9	1.1e-4	−6.3e-6	3.7e-5	7.5e-6	−1.0e-5	−1.5e-5	3.3e-3
10	−3.1e-5	4.4e-5	9.8e-5	−1.9e-5	−1.4e-6	−1.1e-5	3.3e-3

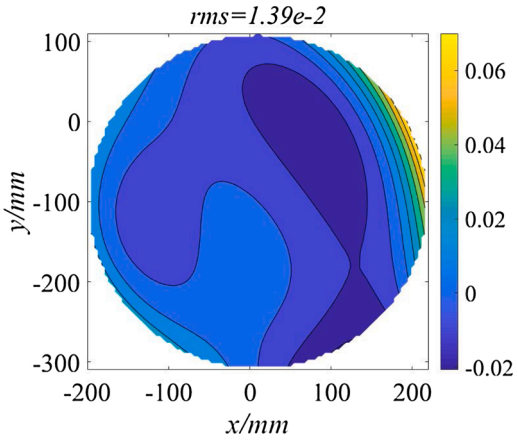

Fig. 4. The diagram of the Zernike polynomial distribution noise with the root mean square value of 1.39e-2 mm.

Table 4
Verification results of the COM program under the Zernike polynomial distribution interference.

Number	Translation errors/*mm*			Rotation errors /°			*rms*(*v*)/*mm*
	Δt_x	Δt_y	Δt_z	$\Delta\theta_x$	$\Delta\theta_y$	$\Delta\theta_y$	
1	1.2e-3	−4.6e-3	2.2e-3	−2.9e-4	9.0e-5	−5.4e-5	8.0e-3
2	1.5e-3	−1.1e-3	**-4.9e-3**	1.4e-5	3.0e-4	−1.3e-4	8.0e-3
3	8.2e-4	5.0e-3	−1.2e-3	−2.4e-6	2.9e-4	1.6e-4	8.0e-3
4	3.5e-3	2.1e-3	−3.3e-3	−7.3e-5	2.9e-4	−2.2e-6	8.0e-3
5	4.3e-3	2.4e-3	−1.7e-3	−7.0e-5	3.0e-4	1.5e-5	8.0e-3
6	7.8e-4	**5.2e-3**	2.7e-4	9.2e-5	**3.1e-4**	−1.6e-4	8.0e-3
7	7.6e-4	2.3e-3	−4.7e-3	**-3.4e-4**	−2.5e-4	1.6e-4	8.0e-3
8	−1.3e-3	−3.9e-3	3.2e-3	−1.9e-4	2.0e-4	1.2e-4	8.0e-3
9	−3.0e-3	3.3e-4	−4.3e-3	3.3e-5	2.9e-4	−1.8e-4	8.0e-3
10	2.9e-3	−3.7e-3	−2.3e-3	−2.3e-4	−1.6e-6	3.0e-4	8.0e-3

accuracy, and can meet the engineering requirement.

4.4. Comparison of extraction efficiency under different conditions

In order to get the accurate results, it is necessary to use as many nodes as possible for finite element simulation analysis. In this way, the data that need to be processed by the extraction algorithm also increases. Therefore, the extraction efficiency of the program is also an important indicator. By adding a timing module to the program, we can obtain the parameter extraction time, which can represent the algorithm efficiency. The efficiency of different algorithms under different conditions is shown in Fig. 5. Conditions 1 to 3 represent simulations without interference, with uniform distributed interference and Zernike polynomial interference, respectively.

It can be clearly seen from Fig. 5 that the efficiency of two algorithms is not affected by the interferences. No matter what kind of interference is added, the calculation time under the same conditions is nearly the same. Furthermore, the calculation time using TFM is much higher than that of COM. And, the calculation time of the TFM fluctuates violently for different conditions, but that of the COM is almost consistent(less than 2 s). These show that the COM algorithm has the characteristics of high efficiency and good stability.

5. Application experiments

In order to verify the actual application effect, the COM is applied to a certain-type deployable telescope which is under development. The finite element model of the segment system is shown in Fig. 6, which is mainly composed of a foldable bottom plate, a motion platform, a co-phasing adjustment device and a segmented mirror which is mounted on the motion platform. Among them, the adjustment device adopts the classic hexapod structure. The model has a total of 66,848 nodes and 39,858 elements, which is mainly composed of 8-nodes hexahedral elements, and a few 6-nodes pentahedral elements for transitioning complex structural.

The relationship between the rigid-body displacement of segmented mirror and the displacements $\vec{l}_n$ of the six linear actuators can be expressed as:

$$\vec{l}_n = \mathbf{A}\vec{u}_n \tag{37}$$

where $\vec{u}_n$ is the rigid-body displacement and **A** is the transfer matrix.

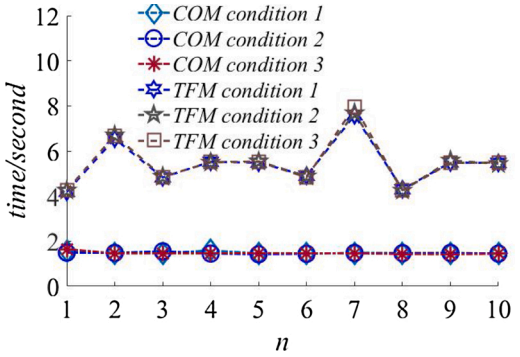

Fig. 5. The efficiency of two algorithms under different conditions.

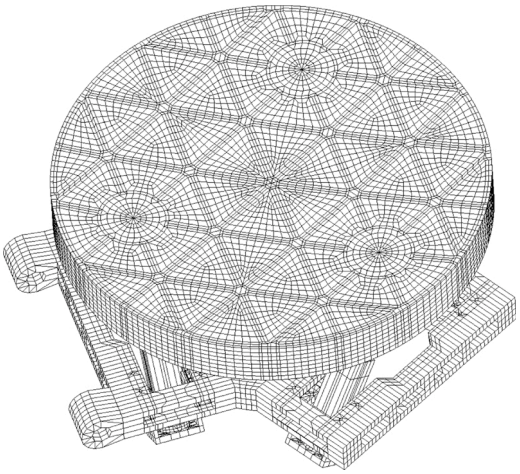

Fig. 6. The finite element model of the segment system.

In order to calibrate the kinematics model shown in Eq. (37), the co-phasing adjustment device (shown in Fig. 7) was developed, and the kinematics calibration test was completed. Because a cube prism is required to feed back the rigid-body displacement of the motion platform, the segmented mirror shown in Fig. 6 is replaced by the cube prism shown in Fig. 7. After the calibration is achieved, the cube prism will be replaced with the segmented mirror. Except for the differences mentioned above, all the structures are equivalent to the finite element model.

The displacement $\overrightarrow{l}_n$ of the linear actuators under the rigid-body motion input can be calculated by using the kinematics model (Eq. (37)), which can be used as the boundary condition for finite element simulation analysis. The nonlinear solver is then called to obtain the node displacement of the segment, which is used as the input of the COM program. And the rigid-body displacement under these nodes displacements is finally acquired. The parameter extraction result is shown in Table 5. It can be seen from Table 5 that the algorithm can separate rigid-body displacement parameters with the precision less than 5‰, which is higher than the finite element

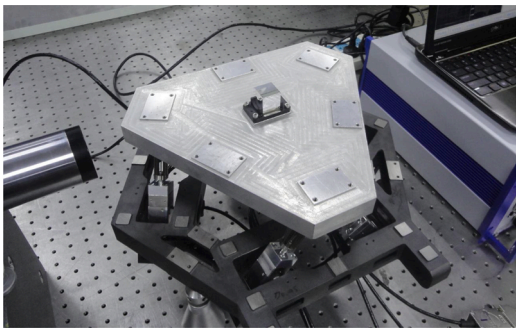

Fig. 7. The co-phasing adjustment device of the segmented mirror.

Table 5
The rigid-body displacement parameters extraction of the segmented co-phasing adjustment simulation results.

Figure	Translation errors/*mm*			Rotation errors /°			*rms*(*v*)/*mm*
	Δt_x	Δt_y	Δt_z	$\Delta\theta_x$	$\Delta\theta_y$	$\Delta\theta_y$	
1	−5.2e-2	−7.5e-2	−7.7e-2	9.8e-2	5.4e-3	−3.8e-3	6.5e-4
2	4.2e-5	6.7e-3	−1.1e-5	−1.6e-3	−1.1e-5	2.8e-4	6.0e-6
3	−2.1e-4	4.9e-3	1.7e-5	−5.5e-4	−3.2e-4	−4.1e-5	4.4e-6
4	−4.0e-5	3.6e-3	6.8e-6	−4.9e-4	−2.3e-5	4.7e-6	2.3e-6

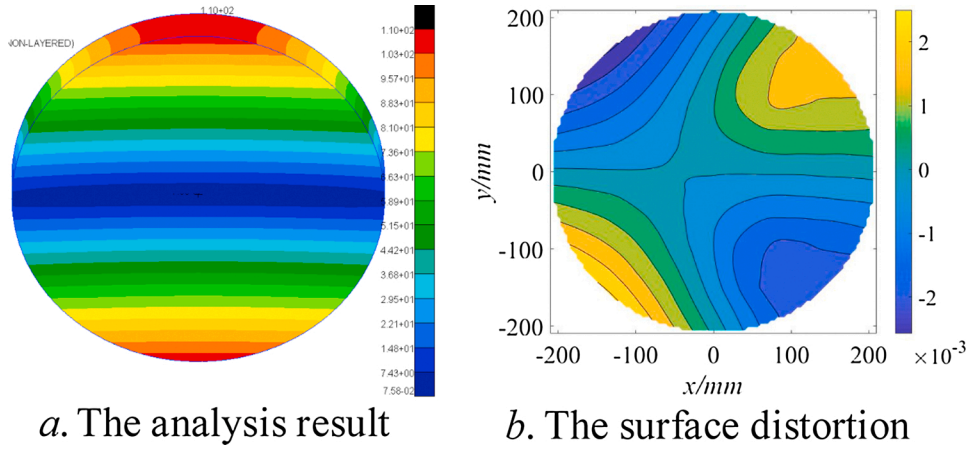

Fig. 8. The analysis results and surface distortion of rotating 30° around *x*-axis.

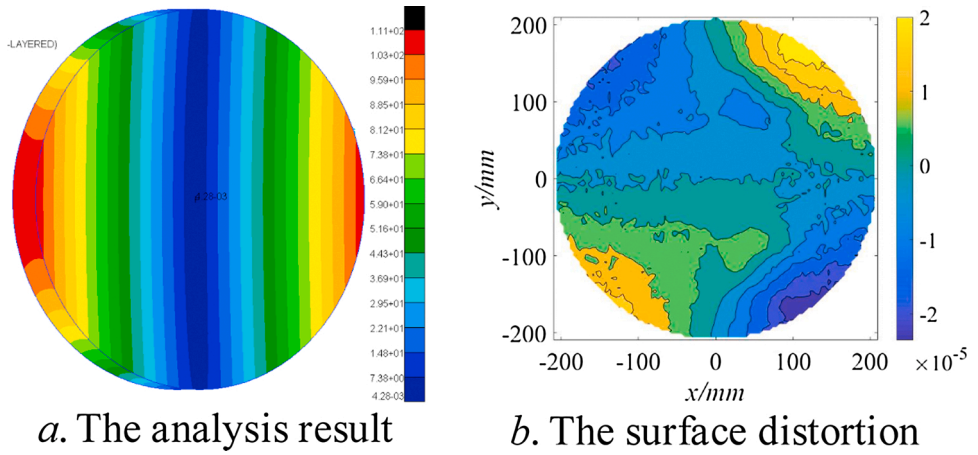

Fig. 9. The analysis results and surface distortion of rotating -30° around *y*-axis.

simulation analysis accuracy, and can meet the actual engineering requirements.

The deformation maps before and after the parameter extraction are shown in Figs. 8–11 to Figs a in Figs. 8–11 are the deformation maps of the finite element simulation analysis, and Figs b, which are surface distortion, are the deformation maps removing the rigid-body displacement. Comparing the Figs. a to the Figs. b, it can be seen that the rigid-body displacement deformation completely obscures the segment surface distortion, and the deformation map of the finite element analysis result cannot truly reflect the surface distortion. Comparing the surface distortion and the calculation residual, we can find that the larger the surface distortion, the lower the solution accuracy. This is also because the rigid-body motion can partially compensate the surface distortion. And the larger the surface distortion, the larger the compensation is. This compensation cannot be separated from the GSDV parameters, and becomes the solving residual. Furthermore, in this application example, 1 *g* gravity along the y-axis is added, which can produce additional rigid-body displacement. All of these are important sources of the COM algorithm error.

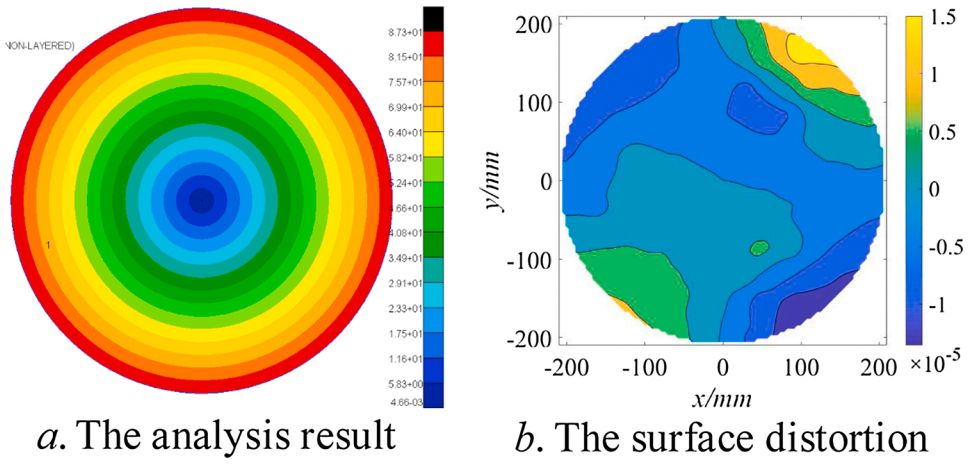

Fig. 10. The analysis results and surface distortion of rotating 24° around *z*-axis.

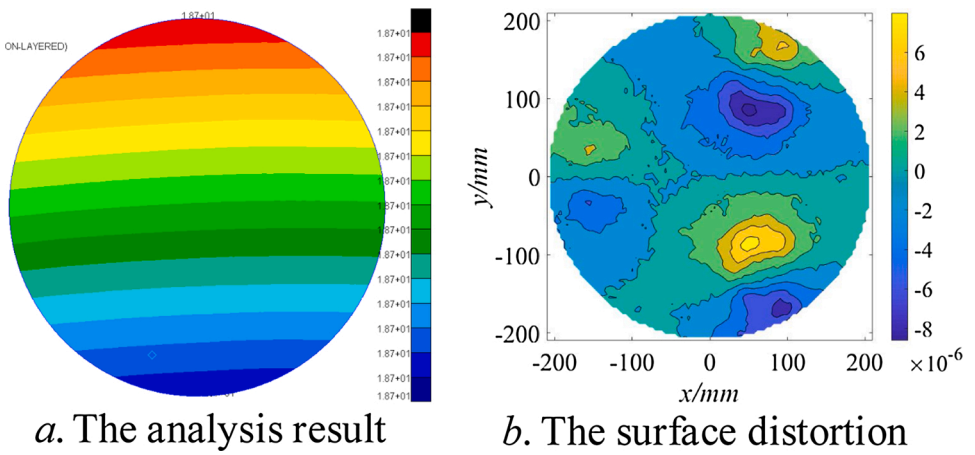

Fig. 11. The analysis results and surface distortion of translating 5 mm, −10 mm, 15 mm along x-axis, y-axis and z-axis respectively.

6. Conclusion

This paper proposes a COM algorithm based on the properties of coordinate transformation matrix, in an attempt to solve the problem that large rigid-body displacement parameters in the simulation analysis results are hard to be extracted. The derivation process of this algorithm was discussed in details, the program was developed, the numerical simulations and application experiments were achieved. The numerical simulations show that compared with the TFM algorithm, this algorithm can improve the calculation efficiency by more than one time without reducing the calculation accuracy, and has the same efficiency and stability for any rigid-body displacement parameters to be extracted. The application experiments show that for a certain-type project under development, the parameters extraction accuracy is better than 5‰, which is higher than the finite element simulation analysis precision, and can further guide the design and optimization of the segment system. The COM algorithm can be applied not only to the regular surface, but also to irregular surfaces, bodies and discrete points, and the coordinate-measuring, although the examples are performed on a mirror surface.

Funding

This work was supported by the National Key Technologies R&D Program of China (Grant No. 2016YFB0500100), National Natural Science Foundation of China (Grant No. 12073028), civil aerospace pre-research project (Grant No. D040101), Equipment pre-research project (Grant No. 30502010501HT01), National Natural Science Foundation of China (Grant No. 11873007).

Declaration of Competing Interest

We declare that we do not have any commercial or associative interest that represents a conflict of interest in connection with the

manuscript entitled, “Large rigid-body displacement parameters extraction of segmented mirror in pose co-phasing adjustment simulation analysis using constrained optimization method”

References

[1] H.S. Yang, X.J. Zhang, Z.L. Li, H. Bao, Y.C. Fan, Technology and development of deployable segmented ultra-large-aperture space remote sensors, Opt. Precision Eng. 26 (6) (2018) 1287–1298.
[2] X.J. Zhang, Y.C. Fan, H. Bao, D.X. Lin, Applications and development of ultra large aperture space optical remote sensors, Opt. Precision Eng. 24 (11) (2016) 2613–2626.
[3] J.M. Oschmann, M. Clampin, H. MacEwen, Special section guest editorial: space telescopes, Opt. Eng. 52 (9) (2013), 091801.
[4] N. Rioux, H. Thronson, L. Feinberg, H.P. Stahl, D. Redding, A. Jones, J. Sturm, C. Collins, A. Liu, A future large-aperture UVOIR space observatory: reference designs, Proc. SPIE. 9602 (2015), 960205.
[5] M. Postman, T. Brown, K. Sembach, M. Giavalisco, W. Traub, K. Stapelfeldt, D. Calzetti, W. Oegerle, R.M. Rich, H.P. Stahl, J. Tumlinson, M. Mountain, R. Soummer, T. Hyde, Advanced technology large-aperture space telescope: science drivers and technology developments, Opt. Eng. 51 (1) (2012), 011007 (2012).
[6] C. Atkinson, S. Texter, R. Keski-Kuha, L. Feinberg, Status of the JWST optical telescope element, Proc. SPIE. 9904 (2016), 990403.
[7] H.S. Yang, X.J. Zhang, Z.L. Li, X.K. Wang, M.M. Xu, Study of the impact of co-phasing errors for segmented primary mirror using nonlinear analysis, Opt. - Int. J. Light Electron. Opt. 191 (2019) 80–88.
[8] H.S. Yang, X.J. Zhang, H. Bao, X.K. Wang, F.M. Chai, Influence of random aspheric parameter errors on the wavefront deformation for segmented primary mirror and its correction, Opt. - Int. J. Light Electron. Opt. 200 (2020), 163406.
[9] H.S. Yang, X.J. Zhang, Z.L. Li, H. Bao, Impact of random segment pose errors for deployable telescope and its tolerance allocation, Opt. Commun. 456 (2020), 124549.
[10] J.L. Jiang, W.R. Zhao, Phasing piston error in segmented telescopes, Opt. Express 24 (17) (2016) 19123–19137.
[11] G.H. Ju, C.X. Yan, Z.Y. Gu, Elimination of the field-dependent aberrations of the JWST-like space telescopes in the multi-field fine-phasing process, Appl. Opt. 56 (10) (2017) 2724–2740.
[12] Y. Bi, J. Cui, J.H. Wu, Q.Q. Hu, One method for mirror surface figure treatment in optical instrument, Opt. Tech. 35 (1) (2009) 10–12.
[13] G.Z. Xu, P. Ruan, New High-precision Algorithm of Surface Parameter for Optical Parabolic Surface [EB/OL] (2019-03-29), 2019, http://kns.cnki.net/kcms/detail/12.1261.TN.20190328.1125.008.html.
[14] Y. Zhang, Z.M. Ding, H.J. Zhao, B.Y. Zou, Rigid-body displacement separation of optics in optical-structural thermal integrated analysis, Infrared Laser Eng. 41 (10) (2012) 2763–2767.
[15] J.Q. Zhang, D.Y. Dong, Q.W. Wu, C.X. Yan, X.J. Zhang, Treatment of surface figure error and rigid body motion for mirror/lens in optical remote sensor, Chin. J. Sci. Instrum. 32 (6) (2011) 242–247.